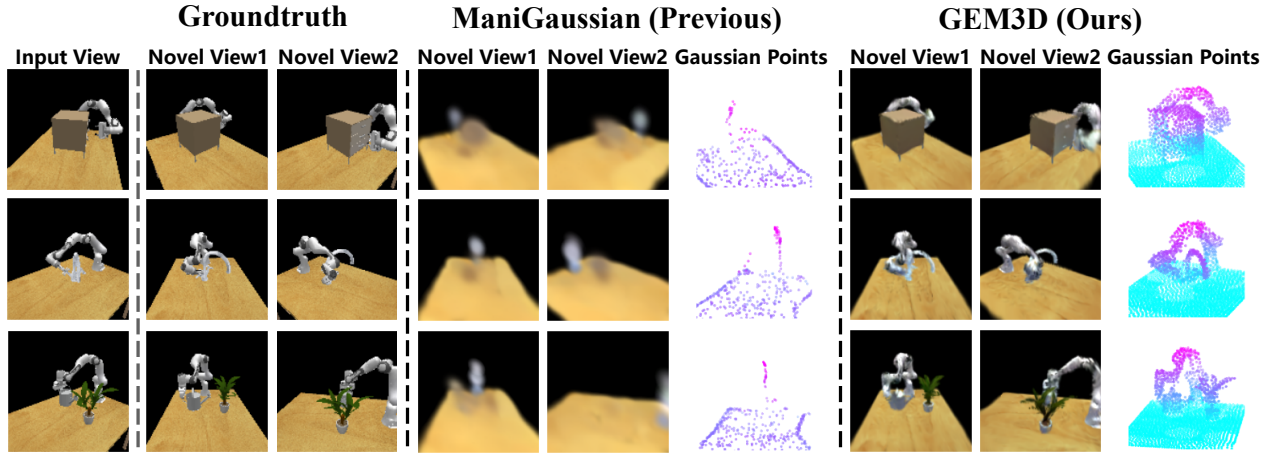


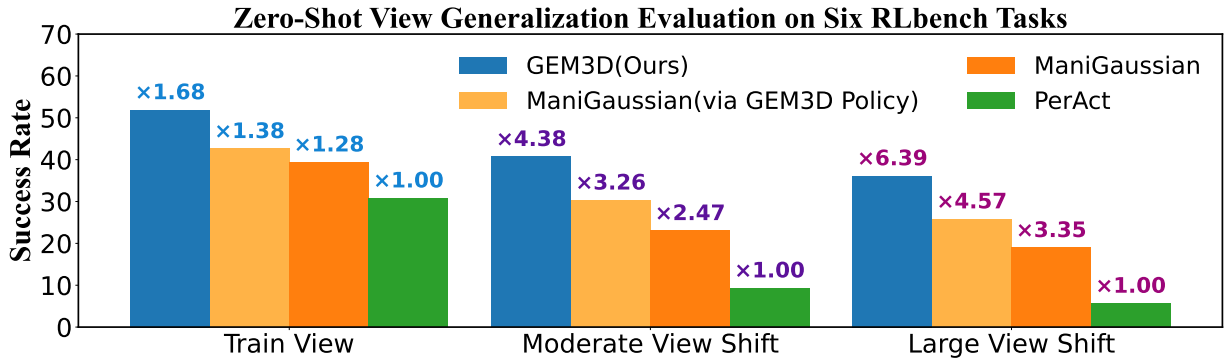
Learning Geometrically-Grounded 3D Visual Representations for View-Generalizable Robotic Manipulation

Di Zhang^{1*} Weicheng Duan^{1*} Dasen Gu¹ Hongye Lu¹ Hai Zhang²
Hang Yu¹ Junqiao Zhao^{1†} Guang Chen¹

¹Tongji University ²The University of Hong Kong



(a) **GEM3D** learns fine-grained 3D representations that enable more accurate novel-view rendering and point cloud reconstruction.



(b) **GEM3D** exhibits strong robustness to viewpoint shifts, maintaining stable visuomotor performance during inference.

Figure 1. We present **GEM3D**, a unified rerepresentation-policy learning framework for view-generalizable robotic manipulation.

Abstract

Real-world robotic manipulation demands visuomotor policies capable of robust spatial scene understanding and strong generalization across diverse camera viewpoints. While recent advances in 3D-aware visual representations have shown promise, they still suffer from several key limitations: (i) reliance on multi-view observations during in-

ference, which is impractical in single-view restricted scenarios; (ii) incomplete scene modeling that fails to capture holistic and fine-grained geometric structures essential for precise manipulation; and (iii) lack of effective policy training strategies to retain and exploit the acquired 3D knowledge. To address these challenges, we present **GEM3D** (**Geometrically-Grounded 3D Manipulation**), a unified representation-policy learning framework for view-generalizable robotic manipulation. **GEM3D** introduces a single-view 3D pretraining paradigm that leverages point cloud reconstruction and feed-forward gaussian splatting

* Equal contribution. Contact {2331922, 2252109}@tongji.edu.cn

† Corresponding author. Contact zhaojunqiao@tongji.edu.cn

Project Website: gem3d-project.github.io/gem3d.github.io/

under multi-view supervision to learn holistic geometric representations. During policy learning, *GEM3D* performs multi-step distillation to preserve the pretrained geometric understanding and effectively transfer it to manipulation skills. We conduct experiments on 12 RLBench tasks, where our approach outperforms the previous state-of-the-art (SOTA) method by **12.7%** in average success rate. Further evaluation on six representative tasks demonstrates the strong zero-shot view generalization of our approach, with the success rate drops by only **22.0%** and **29.7%** under moderate and large viewpoint shifts, respectively, whereas the SOTA method suffers larger decreases of **41.6%** and **51.5%**.

1. Introduction

Learning end-to-end visuomotor policies enables robots to perceive their surroundings and act upon visual understanding [3, 4, 9, 11, 13, 18, 45]. However, real-world environments are often spatially complex and partially occluded, with varying camera viewpoints. Therefore, learning spatially grounded and view-invariant visual representations is essential for developing robust visuomotor policies.

Most existing approaches [10, 19, 41] employ 2D visual encoders to compress images into latent vectors that capture task-relevant states. However, such 2D features lack explicit 3D structural awareness, limiting their effectiveness in spatially intricate manipulation tasks. Recent studies have attempted to address this limitation by leveraging multi-view inputs to learn 3D-aware visual representations [7, 28, 32]. While promising, such methods are often impractical for real-world deployment due to hardware constraints and inference overhead.

More recent efforts [6, 23, 37, 43, 44] introduce single-view 3D perception by incorporating auxiliary reconstruction objectives such as Neural Radiance Fields (NeRFs)[24] or Gaussian Splatting[17]. Although these methods enhance 3D understanding, their scene modeling remains coarse, often failing to recover fine-grained geometric structures that are crucial for precise manipulation (as shown in Fig. 1). Moreover, the resulting visual encoders tend to overfit to specific training viewpoints, leading to degraded generalization in unseen configurations during inference.

To learn more expressive 3D manipulation representations with high-fidelity scene embeddings and strong generalization across varying camera viewpoints, we propose ***GEM3D*** (Geometrically-Grounded 3D Manipulation), a unified representation-policy learning framework that leverages geometrically-grounded 3D representation pretraining on multi-view data and distills the acquired geometric knowledge into a single-view visual policy for downstream robotic manipulation tasks.

GEM3D adopts a three-stage pretraining paradigm to learn expressive 3D scene embeddings: **(i)** From single-

view RGB-D observations, the model encodes the input into a voxel-based *Dense Volumetric Feature*. **(ii)** This volumetric representation is then used to predict skeleton seed points, which are progressively refined into complete point structures via a coarse-to-fine Snowflake process [38], enabling holistic geometric understanding. **(iii)** Guided by the refined points, the *Dense Volumetric Feature* is resampled to predict Gaussian primitives for novel-view rendering under multi-view supervision, capturing fine-grained appearance and texture details. Through this pretraining paradigm, *GEM3D* learns to infer the complete geometry and appearance of a scene from single-view inputs, thereby achieving robust scene understanding and strong view-generalization.

Beyond the generalizable *Dense Volumetric Feature*, developing a robust policy that fully retains the scene understanding capability acquired during pretraining is equally crucial. To this end, we propose a multi-step distillation-based visuomotor policy that can integrate with any pretrained representations, featuring an implicit dynamics-aware design that enhances perception-action consistency. Rather than directly fine-tuning the pretrained encoder, *GEM3D* softly guides the policy’s visual encoder training by aligning its latent features with the pretrained representations, effectively transferring the acquired geometric understanding to manipulation skills.

To evaluate the effectiveness of *GEM3D*, we conduct comprehensive experiments on 12 RLBench manipulation tasks [16]. *GEM3D* achieves a **12.7%** improvement in average success rate over the previous state-of-the-art (SOTA) method ManiGaussian [23]. It also demonstrates strong zero-shot view generalization, with success rates dropping by only **22.03%** and **29.67%** under moderate and large viewpoint shifts, compared to the SOTA method’s **41.62%** and **51.52%** declines. In addition, integrating our distillation-based policy with ManiGaussian-Pretrained representation backbones yields consistent performance gains, indicating its potential for diversified extension to a broader range of backbone architectures. Ablation studies further verify the necessity of each component in our framework.

2. Related Work

2.1. 3D Representation Learning

Recent advances in visuomotor policy learning have explored diverse representation forms, ranging from 2D image features [3, 30] to 3D structures such as voxel grids [33] and point clouds [2, 8, 44]. Among these, novel view synthesis (NVS) has recently gained attention as an auxiliary representation learning objective, as it enables models to infer unseen viewpoints from limited observations—reflecting a holistic understanding of 3D geometry and spatial consistency [17, 22, 24, 27, 31].

However, achieving accurate and generalizable recon-

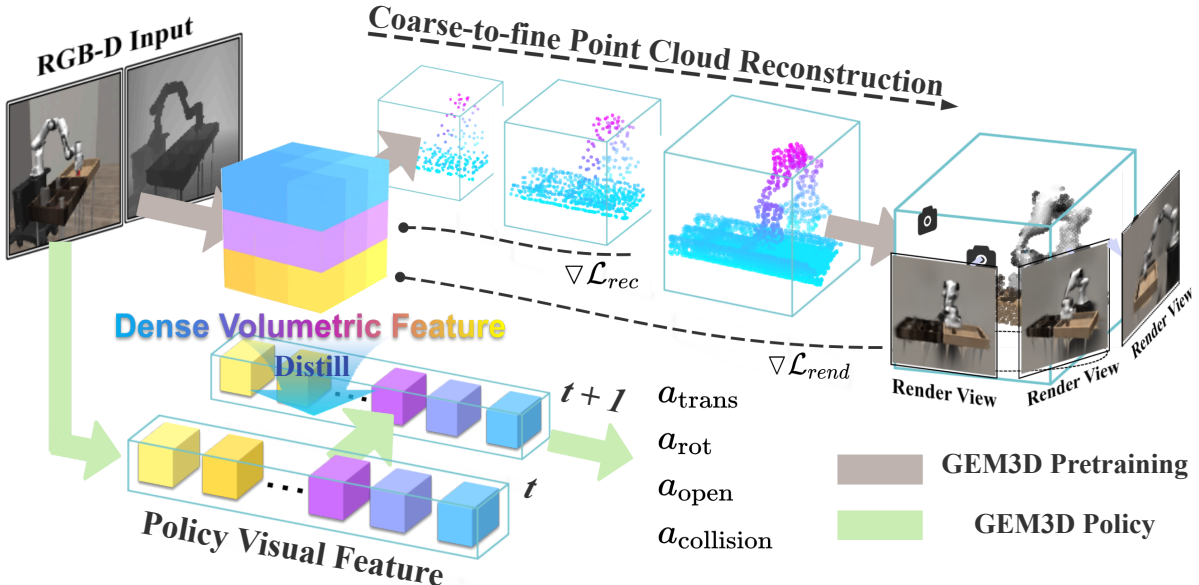


Figure 2. Overview of GEM3D. GEM3D comprises two key components: (1) **GEM3D Pretraining**, which learns holistic 3D representations through auxiliary scene reconstruction tasks; and (2) **GEM3D Policy**, which distills the pretrained 3D visual representations into a visuomotor policy for view-generalizable manipulation.

struction remains challenging for existing NVS paradigms. Classical methods such as NeRFs [24] and Gaussian Splatting [17] often struggle to generalize beyond the training distribution, leading to degraded rendering quality in novel scenes or viewpoints. More recent feed-forward Gaussian Splatting approaches—ImageSplatter [34], VoxSplat [29], and PixelSplat [1]—improve generalization but remain unstable in dynamic environments, exhibiting noticeable degradation in reconstructed geometry and texture (see Fig. 1). These limitations highlight the need for a NVS framework that achieves both high-fidelity reconstruction and robust generalization across diverse robotic scenes.

2.2. Visuomotor Policy Learning

To effectively leverage the benefits of auxiliary representation learning tasks, recent visuomotor policy research can be categorized into two major training paradigms:

(i) **Pretrain-Finetune**. These methods leverage visual encoders that are pretrained on large-scale 2D or 3D perception datasets and subsequently finetuned for downstream control tasks [28, 36, 39, 40, 42]. However, domain discrepancies between pretraining and downstream control tasks can lead to suboptimal transfer, and even degrade policy learning, as observed in [12, 14].

(ii) **Joint-Training**. This paradigm jointly optimizes visuomotor policies with auxiliary representation objectives, such as NVS [23, 43]. Yet, the optimization tends to be imbalanced: the representation gains little from auxiliary tasks, while the policy overfits to training viewpoints and generalizes poorly to unseen camera poses.

In contrast to prior works, we propose a multi-step distillation framework that softly guides the policy encoder training with pretrained 3D representations, effectively preserving geometric knowledge acquired during pretraining.

3. Method

Our goal is to learn a voxel-based 3D visual representation through pretraining and subsequently distill the acquired 3D knowledge into a visuomotor policy for view-generalizable robotic manipulation. In the following, we outline the overall framework of GEM3D. Sec. 3.1 details the pretraining pipeline and Sec. 3.2 presents the policy learning strategy. An overview is shown in Fig. 2.

3.1. Geometrically-Grounded Pretraining

GEM3D’s pretraining pipeline consists of three main components: (i) a **3D Feature Extraction** module that encodes single-view RGB-D observations into *dense volumetric features*; (ii) a **Point Cloud Reconstruction** objective that learns holistic 3D scene geometry; and (iii) a **Feed-forward 3D Gaussian Splatting** module that captures fine-grained texture through multi-view supervision. The detailed pipeline is illustrated in Fig. 3.

3.1.1. 3D Feature Extraction

As shown in Fig. 3a, the feature extraction module takes a single-view RGB-D input $o^t = \{\mathcal{I}^t, \mathcal{D}^t, \mathcal{K}^t\}$ and processes it as follows:

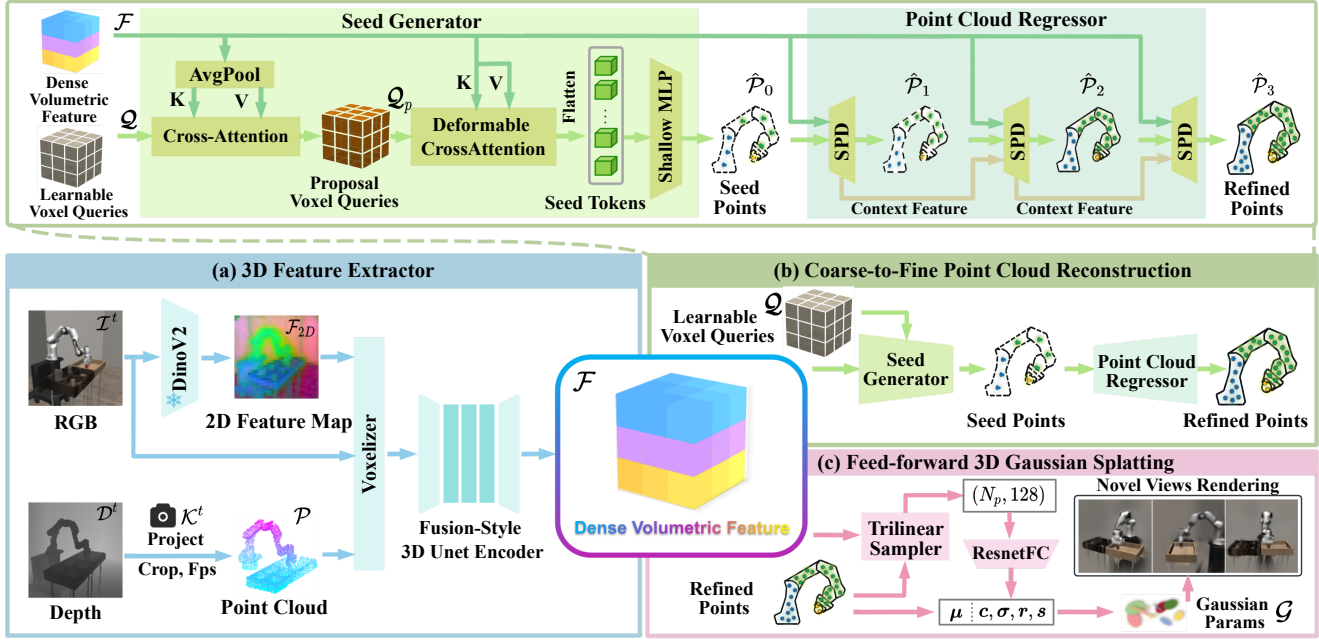


Figure 3. GEM3D Pretraining Pipeline. (a) encoding single-view RGB-D observations into volumetric features, (b) progressively reconstructing scene geometry in a coarse-to-fine Snowflake [38] manner, and (c) learning fine-grained texture details through Gaussian-splatting-based novel view rendering.

- The depth map \mathcal{D}^t is back-projected using the camera parameters \mathcal{K}^t , followed by cropping and farthest point sampling to obtain the point cloud \mathcal{P} .
- The RGB image \mathcal{I}^t is encoded by a pretrained DI-NOv2 [25] model to extract pixel-wise 2D features \mathcal{F}_{2D} , which are then projected onto \mathcal{P} to enrich the point cloud with visual semantics.
- The resulting semantically enriched point cloud is voxelized into occupancy and feature volumes, which are subsequently fused through a 3D U-Net [5] to produce the *Dense Volumetric Feature* $\mathcal{F} \in \mathbb{R}^{D^3 \times 128}$, where D denotes the voxel resolution, and 128 corresponds to the feature dimension.

This process encodes the single-view RGB-D observation into a dense voxel-based 3D representation \mathcal{F} that jointly captures geometric structure and visual semantics.

3.1.2. Coarse-to-Fine Point Cloud Reconstruction

To enable the **holistic geometric understanding** of the volumetric feature \mathcal{F} , we introduce a coarse-to-fine reconstruction module that first predicts sparse seed points and then progressively refines them into a dense point cloud (Fig. 3b).

Seed Points Generation. To capture the key structural points necessary for reconstructing the full scene, we initialize a *learnable voxel query set* $\mathcal{Q} \in \mathbb{R}^{d^3 \times 128}$ (with $d \ll D$ to reduce computational overhead) and apply a two-stage attention mechanism to aggregate multi-scale spatial features from the volumetric representation \mathcal{F} :

- *Coarse Cross-Attention:* We first downsample \mathcal{F} with average pooling to obtain a low-resolution feature $\mathcal{F}_{\text{down}} \in \mathbb{R}^{d^3 \times 128}$, which only preserves the overall spatial structure of the scene. And then we perform cross-attention between \mathcal{Q} and $\mathcal{F}_{\text{down}}$ to obtain *proposal queries* \mathcal{Q}_p that capture coarse spatial relationships.
- *3D Deformable Cross-Attention:* To further enrich \mathcal{Q}_p with fine-grained geometric cues, we apply a 3D deformable cross-attention module between \mathcal{Q}_p and \mathcal{F} , following [20, 46]. This enables efficient aggregation of local geometric details from \mathcal{F} to the query features. Implementation details are provided in Appendix A.

This process yields a set of *seed tokens*, which are decoded by a shallow MLP to produce seed point coordinates $\hat{\mathcal{P}}_0 \in \mathbb{R}^{d^3 \times 3}$.

Point Cloud Recovery. Starting from the seed points $\hat{\mathcal{P}}_0$, we follow the SnowflakeNet [38] and employ a *Snowflake Point Deconvolution* (SPD) block to progressively refine the point set. At each stage i :

- The parent points $\hat{\mathcal{P}}_i \in \mathbb{R}^{N_i \times 3}$ (N_i denotes the point number at stage i) query the volumetric feature \mathcal{F} via trilinear interpolation at their coordinates to obtain point features $\mathcal{F}_i \in \mathbb{R}^{N_i \times 128}$.
- Given $\hat{\mathcal{P}}_i$, \mathcal{F}_i and current context features \mathcal{F}_i^c (*the intermediate output of the previous SPD stage, omitted for the first iteration*) as input, the SPD block upsamples each point by a factor of r , producing r displacement vectors for each parent point $\Delta\mathcal{P}_i \in \mathbb{R}^{r \times N_i \times 3}$ and outputs the updated context features \mathcal{F}_{i+1}^c .

- Each parent point is duplicated r times and displaced by the predicted offsets $\Delta\mathcal{P}_i$ to form the refined child points $\hat{\mathcal{P}}_{i+1} \in \mathbb{R}^{N_{i+1} \times 3}$, where $N_{i+1} = r \times N_i$.

To supervise reconstruction with holistic scene geometry, we fuse multi-view ground-truth point clouds into a complete set $\mathcal{P}_{\text{full}}$. At each refinement stage i , we use farthest point sampling to sample a subset $\mathcal{P}_i \subset \mathcal{P}_{\text{full}}$ with a size comparable to that of the predicted set $\hat{\mathcal{P}}_i$, and supervise the refinement using the *Chamfer distance* L_2 :

$$\mathcal{L}_{\text{rec}} = \sum_{i=0}^3 \left(\frac{1}{|\hat{\mathcal{P}}_i|} \sum_{\hat{\mathbf{p}} \in \hat{\mathcal{P}}_i} \min_{\mathbf{p} \in \mathcal{P}_i} \|\hat{\mathbf{p}} - \mathbf{p}\|_2^2 + \frac{1}{|\mathcal{P}_i|} \sum_{\mathbf{p} \in \mathcal{P}_i} \min_{\hat{\mathbf{p}} \in \hat{\mathcal{P}}_i} \|\mathbf{p} - \hat{\mathbf{p}}\|_2^2 \right) \quad (1)$$

3.1.3. Feed-forward 3D Gaussian Splatting

Based on the reconstructed dense point cloud $\hat{\mathcal{P}}$, we further integrate a feed-forward 3D Gaussian Splatting pipeline that performs novel-view rendering and **captures fine-grained texture details** under multi-view supervision. (Fig. 3 (c))

The Gaussian centers μ are directly given by the refined points $\hat{\mathcal{P}} \in \mathbb{R}^{N_p \times 3}$. At these locations, we sample Gaussian features $\mathcal{F}_G \in \mathbb{R}^{N_p \times 128}$ from the dense volumetric field \mathcal{F} via trilinear interpolation, and feed them into a ResNetFC network to regress the remaining non-positional Gaussian parameters—including color, opacity, rotation and scale:

$$\{c, \sigma, r, s\} = \text{ResNetFC}(\mathcal{F}_G) \quad (2)$$

The resulting 3D Gaussian parameters $\mathcal{G} = [\mu, c, \sigma, r, s]$ are employed in a differentiable renderer to synthesize novel-view images $\hat{\mathcal{I}}_v^t$, which are supervised by the corresponding multi-view RGB observations \mathcal{I}_v^t using a *focal loss* [21], which places greater emphasis on dynamic and visually ambiguous regions:

$$\mathcal{L}_{\text{rend}} = \text{FocalLoss}(\hat{\mathcal{I}}_v^t, \mathcal{I}_v^t). \quad (3)$$

3.2. Distillation-based Policy Learning

Instead of directly finetuning the pretrained visual encoder obtained from Sec. 3.1.1, which may disrupt the learned geometric representations. As shown in Fig. 4, we initialize a separate policy encoder to process the single-view RGB-D observation o^t into latent tokens \mathbf{x}^t . Meanwhile, the frozen *Pretrained 3D Feature Extractor* produces the corresponding *dense volumetric feature* \mathcal{F}^t , which is subsequently patchified into reference tokens $\tilde{\mathbf{x}}^t$. A cosine-similarity-based distillation loss is then applied to align the latent and reference tokens (as shown in Fig. 4).

Since we adopt end-effector position control, the robot action a_t is implicitly embedded within the next latent state \mathbf{x}^{t+1} . To equip the policy with dynamic understanding, we introduce an implicit latent dynamics model that predicts \mathbf{x}^{t+1} from the current latent state \mathbf{x}^t , together with proprioception and language embeddings. The action a_t is then

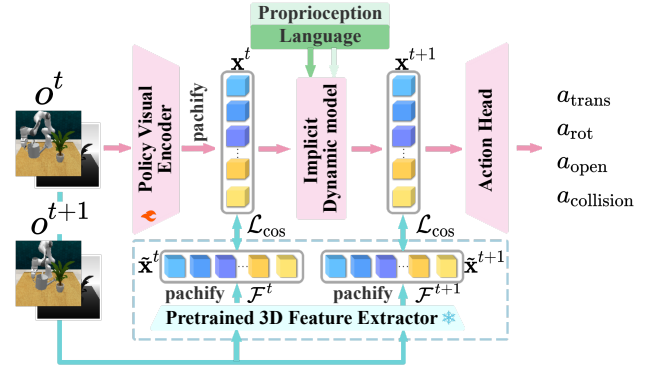


Figure 4. GEM3D Policy. A multi-step distillation-based policy learning framework.

decoded from \mathbf{x}^{t+1} through an action head. This design features two benefits: (i) improve the decision explainability by modeling temporal transitions in the latent space; and (ii) further enables multi-step latent distillation to regularize the policy’s temporal consistency, formulated as:

$$\mathcal{L}_{\text{distill}} = \mathcal{L}_{\text{cos}}(\mathbf{x}^t, \tilde{\mathbf{x}}^t) + \mathcal{L}_{\text{cos}}(\mathbf{x}^{t+1}, \tilde{\mathbf{x}}^{t+1}) \quad (4)$$

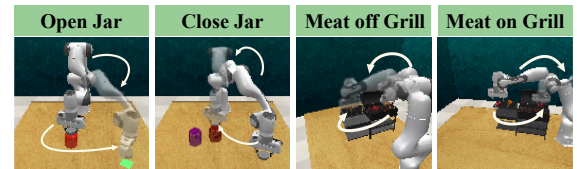
We train the policy via imitation learning using expert actions as supervision. The overall policy training objective is formulated as:

$$\mathcal{L}_{\text{policy}} = \|\mathbf{a}_t - \mathbf{a}_t^*\|_2^2 + \lambda_{\text{distill}} \mathcal{L}_{\text{distill}}, \quad (5)$$

4. Experiments

4.1. Experimental Setup

Evaluation setup. We evaluate our method on RL-Bench [16], covering 12 tasks across 9 scenes with varying task instructions. These tasks span diverse manipulation challenges and require both fine-grained control and strong spatial reasoning, as illustrated in Fig. 5a.



(a) RLBench task examples.

Train View	Moderate Shift	Large Shift
0 °	-30 ° ~ 30 °	60 ° ~ 90 °

(b) View-generalization evaluation settings.

Figure 5. Examples of our evaluation setup.

During pretraining, multi-view observations are captured from 8 uniformly distributed surrounding cameras, with 50 trajectories per scene ($50 \times 9 = 450$ episodes in total). For

Table 1. Comparison of *GEM3D* with state-of-the-art methods on all 12 RLBench tasks (SR%). **Bold** numbers denote the best performance, and underlined numbers denote the second best.

Methods	Avg. SR (%) \uparrow	Avg. Rank \downarrow	Close Jar	Open Drawer	Meat off Grill	Turn Tap	Water Plants
<i>PerAct</i>	21.9 ± 5.3	4.58	19.0 ± 4.6	38.7 ± 13.7	28.3 ± 4.7	43.7 ± 4.7	8.3 ± 2.3
<i>GNFactor</i>	29.2 ± 18.4	3.33	<u>32.0 ± 16.8</u>	51.7 ± 13.5	32.0 ± 10.5	40.7 ± 10.7	<u>22.0 ± 4.4</u>
<i>ManiGaussian</i>	31.5 ± 8.5	3.08	27.3 ± 16.4	<u>57.3 ± 1.5</u>	30.0 ± 11.3	<u>44.0 ± 10.5</u>	19.3 ± 9.0
<i>ManiGaussian (w Distill)</i>	<u>33.3 ± 10.4</u>	<u>3.00</u>	31.0 ± 12.1	54.3 ± 12.5	<u>35.3 ± 9.8</u>	42.7 ± 14.6	16.3 ± 8.7
<i>GEM3D (Ours)</i>	44.2 ± 6.2	1.00	44.7 ± 3.2	65.7 ± 4.5	44.3 ± 3.1	54.0 ± 7.2	32.7 ± 3.5
Methods	Phone on Base	Put Money in Safe	Place Wine	Stack Blocks	Open Jar	Meat on Grill	Take Money out Safe
<i>PerAct</i>	51.3 ± 11.9	10.7 ± 0.6	3.0 ± 1.0	4.0 ± 0.0	26.7 ± 9.1	16.0 ± 7.9	13.7 ± 2.9
<i>GNFactor</i>	62.0 ± 5.6	11.0 ± 10.5	5.7 ± 2.1	3.7 ± 1.2	35.7 ± 6.4	35.0 ± 6.1	19.0 ± 4.0
<i>ManiGaussian</i>	<u>66.3 ± 12.5</u>	5.7 ± 3.5	<u>8.0 ± 2.6</u>	2.0 ± 1.7	<u>38.3 ± 9.0</u>	30.7 ± 12.9	<u>49.3 ± 10.5</u>
<i>ManiGaussian (w Distill)</i>	64.3 ± 16.2	<u>20.3 ± 9.2</u>	5.3 ± 3.5	<u>5.0 ± 2.6</u>	33.7 ± 9.5	<u>48.7 ± 2.9</u>	43.0 ± 23.4
<i>GEM3D (Ours)</i>	67.3 ± 1.5	29.7 ± 2.9	11.7 ± 4.0	7.7 ± 2.9	40.0 ± 5.6	61.0 ± 22.1	72.0 ± 13.7

policy learning, each task is trained using 20 expert demonstrations collected from a fixed front-view camera.

Evaluation metrics. We evaluate policy performance using the task success rate (SR), defined as 1 for success and 0 for failure per episode, without partial credit.

For fair comparison, each model is trained with three fixed random seeds (0, 1, 2). To mitigate overfitting, checkpoints at both 80% and the final training step are evaluated, and the better result per seed is selected. Each seed is tested on 100 different settings per task, including 178 variations in language, object position, and color. We report the mean and standard deviation of SR across all seeds.

To assess view generalization, we perform zero-shot evaluations under three levels of camera viewpoint shifts (as shown in Fig. 5b):

- *No Shift*: Same viewpoint as training.
- *Moderate Shift*: Camera relocated within 30° around the robot base.
- *Large Shift*: Significant viewpoint variations between 60° and 90° .

Baselines. We adopt **PerceiverIO** [15] as our policy backbone for its simplicity and compatibility with discrete token-based input-output representations. For fair comparison, we consider prior methods that also employ the PerceiverIO architecture as their policy backbone, including: (i) **PerAct** [33], which directly utilizes voxel-based 3D representations; (ii) **GNFactor** [43], which incorporates NeRFs as an auxiliary representation learning objective; and (iii) **ManiGaussian** [23], which leverages 3D Gaussian Splatting for representation learning and jointly trains it with the policy.

To further assess our distillation-based policy learning framework, we pair the ManiGaussian representation module with our training strategy, denoted as (iv) **ManiGaussian (w Distill)**, and additionally compare its pretraining

quality against *GEM3D*.

Implementation details. We apply SE(3) augmentations to the input point cloud following prior works [33, 35]. *GEM3D* is pretrained for 100K iterations on two NVIDIA RTX3090 GPUs, taking approximately four to five days. Each policy is then trained for 12K iterations on a single RTX3090 GPU, requiring about three to four hours per task.

Additional implementation and experimental setup details are provided in the Appendix B.

4.2. Experimental Results

4.2.1. Comparison with State-of-the-Art Methods

We compare *GEM3D* with baseline methods on 12 RL-Bench tasks, with each model trained independently per task. The results are shown in Tab. 1, *GEM3D* achieves the highest overall performance, attaining an average success rate of **44.2%** and an absolute gain of **12.7%** over *ManiGaussian*, the previous State-of-the-Art (SOTA) method.

Furthermore, Tab. 2 reports the zero-shot success rates under varying degrees of viewpoint shifts on six representative tasks, together with the relative performance drop compared to the training view. *GEM3D* exhibits only **22.03%** and **29.67%** declines under *moderate* and *large* shifts, respectively—significantly lower than the **41.62%** and **51.52%** drops observed in *ManiGaussian*. Under large viewpoint shifts, our method achieves up to **6 \times** higher success rates than *PerAct* (see Fig. 1).

Notably, although the distilled variant *ManiGaussian (w distill)* shows slightly improved robustness over its original version, its performance remains far below that of *GEM3D*. This suggests that while our distillation-based policy training helps mitigate performance degradation under unseen viewpoint shifts, holistic 3D representation learning through stronger pretraining is the key to achieving view-generalizable visuomotor policies.

Table 2. Result of zero-shot view generalization on six RLBench tasks under two view-shift settings (SR%). **Bold** numbers denote the best performance, and \downarrow indicates the relative performance drop compared to the training view.

Methods		Close Jar	Meat off Grill	Turn Tap	Phone on Base	Open Jar	Meat on Grill	Avg.
Moderate Shift	<i>PerAct</i>	7.7 ± 9.9 (59.65% \downarrow)	19.7 ± 7.2 (30.56% \downarrow)	14.0 ± 7.2 (67.94% \downarrow)	0.3 ± 0.6 (99.35% \downarrow)	2.0 ± 1.7 (92.50% \downarrow)	12.3 ± 9.6 (22.92% \downarrow)	9.3 ± 7.4 (69.80% \downarrow)
	<i>ManiGaussian</i>	15.3 ± 15.9 (43.91% \downarrow)	17.0 ± 12.1 (43.33% \downarrow)	32.3 ± 2.3 (26.52% \downarrow)	30.7 ± 18.6 (53.76% \downarrow)	18.3 ± 2.5 (52.18% \downarrow)	24.3 ± 10.1 (20.67% \downarrow)	23.0 ± 7.3 (41.62% \downarrow)
	<i>ManiGaussian</i> (<i>w Distill</i>)	20.3 ± 10.3 (34.41% \downarrow)	23.7 ± 2.3 (33.01% \downarrow)	34.0 ± 9.8 (20.32% \downarrow)	40.0 ± 22.6 (37.82% \downarrow)	21.7 ± 3.2 (35.64% \downarrow)	42.3 ± 7.0 (13.02% \downarrow)	30.3 ± 9.7 (28.87% \downarrow)
	<i>GEM3D</i> (<i>ours</i>)	33.7 ± 8.5 (24.62% \downarrow)	33.0 ± 5.0 (25.56% \downarrow)	47.4 ± 8.4 (14.88% \downarrow)	48.3 ± 13.6 (28.22% \downarrow)	34.3 ± 4.0 (14.18% \downarrow)	47.0 ± 14.8 (22.95% \downarrow)	40.7 ± 7.7 (22.03% \downarrow)
Large Shift	<i>PerAct</i>	2.8 ± 3.4 (85.11% \downarrow)	15.7 ± 3.1 (44.69% \downarrow)	9.7 ± 4.3 (77.86% \downarrow)	1.0 ± 2.0 (98.05% \downarrow)	3.3 ± 4.1 (87.51% \downarrow)	4.8 ± 3.8 (69.81% \downarrow)	6.2 ± 5.5 (79.87% \downarrow)
	<i>ManiGaussian</i>	10.3 ± 14.2 (62.20% \downarrow)	16.3 ± 8.4 (45.57% \downarrow)	27.0 ± 7.0 (38.64% \downarrow)	23.7 ± 16.0 (64.32% \downarrow)	21.5 ± 6.0 (43.91% \downarrow)	16.0 ± 6.2 (47.83% \downarrow)	19.1 ± 6.1 (51.52% \downarrow)
	<i>ManiGaussian</i> (<i>w Distill</i>)	21.5 ± 9.2 (45.16% \downarrow)	16.3 ± 6.9 (67.92% \downarrow)	32.0 ± 8.6 (29.69% \downarrow)	33.7 ± 13.1 (41.97% \downarrow)	23.0 ± 12.0 (62.38% \downarrow)	28.2 ± 8.0 (53.42% \downarrow)	25.8 ± 6.6 (39.43% \downarrow)
	<i>GEM3D</i> (<i>ours</i>)	30.2 ± 7.1 (32.46% \downarrow)	26.0 ± 5.8 (41.35% \downarrow)	45.3 ± 6.3 (19.05% \downarrow)	39.0 ± 13.2 (42.08% \downarrow)	35.8 ± 7.7 (10.42% \downarrow)	40.3 ± 6.8 (33.88% \downarrow)	36.1 ± 7.1 (29.67% \downarrow)

Table 3. Multi-task results on four RLBench tasks (SR%). **Bold** numbers denote the best performance, and \downarrow indicates the relative performance drop compared to the single-task training setting.

Methods	Train View	Moderate Shift	Large Shift
<i>PerAct</i>	26.1 ± 17.5 (24.1% \downarrow)	6.4 ± 4.5 (11.1% \downarrow)	5.6 ± 3.6 (16.1% \uparrow)
<i>ManiGaussian</i> (<i>w Distill</i>)	47.1 ± 5.8 (0.4% \downarrow)	30.7 ± 8.1 (3.8% \downarrow)	26.5 ± 7.7 (10.7% \downarrow)
<i>GEM3D</i> (<i>ours</i>)	52.9 ± 6.4 (1.7% \uparrow)	41.2 ± 9.6 (6.9% \downarrow)	36.4 ± 9.0 (3.7% \downarrow)

4.2.2. Multi-task Evaluation

To further validate the language-following ability and task-level generalization of *GEM3D*, we train a unified model using a mixture of four RLBench task datasets.

The multi-task average success rates and their relative decreases compared to the single-task setting are reported in Tab. 3. While the original *PerAct* baseline exhibits a substantial drop on the train view and even shows policy collapse under shifted viewpoints, our policy shows only a modest decline, with the largest decrease being just 6.9% compared to its single-task performance. This demonstrates that our geometrically grounded representation also facilitates clearer task distinction and more reliable instruction following.

Further explanations of task selection and per-task results are provided in Appendix C.

4.2.3. Qualitative Analysis of Scene Reconstruction

High-fidelity scene reconstruction serves as a strong indicator of a model’s grasp of 3D geometry and appearance. As illustrated in Fig. 1, our method reconstructs sharper structures and produces more consistent novel views, while *ManiGaussian* suffers from blurred textures and geomet-

Table 4. Comparison of scene reconstruction quality. Larger PSNR and SSIM indicate better image fidelity, while lower Chamfer L_2 indicates higher point cloud geometric accuracy.

Methods	Tasks	PSNR \uparrow	SSIM \uparrow	Chamfer $L_2 \downarrow$
<i>ManiGaussian</i>	Open Drawer	16.24	0.3926	0.04035
	Turn Tap	15.84	0.3741	0.05148
	Water Plants	16.07	0.3846	0.04352
Avg		16.05	0.3838	0.04511
<i>GEM3D</i> (<i>ours</i>)	Open Drawer	23.54	0.8259	0.01541
	Turn Tap	22.92	0.8123	0.01708
	Water Plants	22.93	0.8025	0.01613
Avg		23.13	0.8136	0.01621

ric distortions. These results highlight that our geometrically grounded 3D representations yield a more holistic and viewpoint-robust understanding of the scene.

Furthermore, we report quantitative metrics for the three scenes in Fig. 1 (see Tab. 4), including PSNR and SSIM for image quality and Chamfer L_2 for geometric accuracy. *GEM3D Pretraining* consistently outperforms the pretraining method of *ManiGaussian*, achieving average improvements of +7.08 dB in PSNR, +0.4298 in SSIM, and -0.0289 in Chamfer L_2 , demonstrating its stronger ability to capture both visual fidelity and geometric consistency.

4.3. Ablations

4.3.1. Ablation on GEM3D Pretraining

In our *GEM3D Pretraining* module, we highlight three essential designs that jointly enhance geometric reconstruction and texture rendering:

- **Deformable cross-attention (DCA)** ensures efficient and precise seed generation while preserving spatial integrity.

- **Snowflake-style coarse-to-fine reconstruction** expands and refines point sets over three upsampling stages, yielding progressively denser geometric structures.
- **Focal loss** emphasizes supervision on dynamic and ambiguous regions, enhancing robustness to motion-induced appearance and geometry changes.

We demonstrate the importance of these components through qualitative ablations (see Fig. 6). (i) In the *w/o DCA* variant, deformable cross-attention is replaced with standard cross-attention between dense and downsampled volumetric features, leading to the loss of fine spatial cues. (ii) The *w/o snowflake* variant adopts a single-step reconstruction, preventing the model from progressively refining geometric details. (iii) The *w/o focal loss* setting replaces focal loss with a plain MSE objective for Gaussian rendering, reducing supervisory emphasis on dynamic or ambiguous regions. Across all cases, removing any individual component results in clear degradation—robot arms collapse, complex plant structures fail to reconstruct, and texture consistency deteriorates—highlighting the essential role each module plays in the overall design.

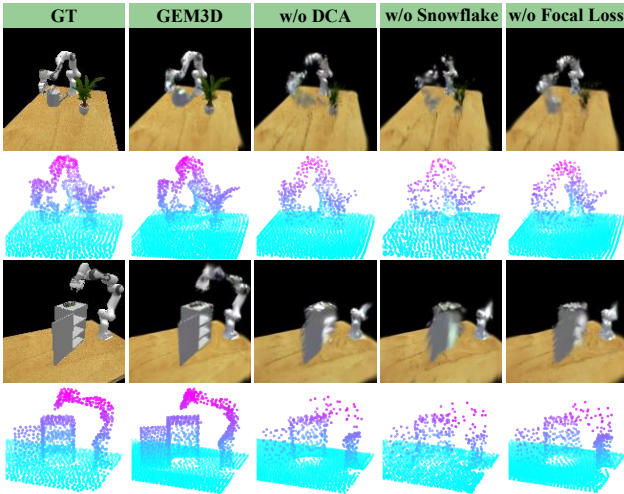


Figure 6. Qualitative ablation on *GEM3D Pretraining* designs

4.3.2. Ablation on the Number of Pretraining Viewpoints

In our experiments, we use multi-view observations from eight surrounding cameras for pretraining. While effective, this configuration is often impractical in real-world deployment. To evaluate the dependence on view count, we vary the number of pretraining views and conduct multi-task training on Phone on Base, Meat on Grill, and Turn Tap. Tab. 5 summarizes the average success rates under different view settings, including a “0-view” setting where the *Feed-forward Gaussian Splatting Rendering* module is disabled.

We observe that *GEM3D Pretraining* is largely insensitive to the number of available views: reducing the pretraining setup from eight to two cameras leads to only marginal

Table 5. Ablations on pretraining viewpoint numbers (SR%).

Modules	Train View	Moderate Shift	Large Shift
Train View	8	58.8 \pm 6.0	45.9 \pm 8.4
	4	54.6 \pm 4.9	42.4 \pm 6.6
	2	54.9 \pm 5.1	40.3 \pm 5.1
w/o gaussian splatting		47.2 \pm 7.4	33.4 \pm 6.1
			30.8 \pm 5.8

declines in success rates across all viewpoint conditions. In contrast, removing the Gaussian Splatting module yields a pronounced performance drop of nearly 10%. This indicates that Gaussian Splatting not only captures fine-grained appearance details but also enforces spatial consistency across viewpoints, enabling strong performance even under limited multi-view supervision.

4.3.3. Ablation on GEM3D Policy

In this section, we perform an ablation study on the effectiveness of the *GEM3D Policy* architecture. Under the same experimental setup as Sec. 4.3.2, we compare two variants:

- *Single-step Distillation*: Representation alignment is applied only at the input token level, with the $t+1$ latent distillation step removed from the multi-step pipeline.
- *Pretrain-Finetune*: A conventional baseline where the pretrained encoder is directly fine-tuned on downstream tasks without distillation.

Tab. 6 reports the average success rates across three tasks. The results indicate that incorporating distillation at the $t+1$ step improves temporal consistency in the latent dynamics, leading to noticeably stronger policy performance. In contrast, the conventional pretrain-finetune paradigm suffers from representation drift caused by the domain gap between pretraining and downstream tasks [12, 26], resulting in substantially reduced manipulation success.

Table 6. Ablations on *GEM3D* policy training (SR%).

Methods	Train View	Moderate Shift	Large Shift
<i>Pretrain-Finetune</i>	32.2 \pm 11.1	21.1 \pm 6.7	15.1 \pm 6.8
<i>Single-step Distillation</i>	54.6 \pm 7.6	41.7 \pm 9.0	37.7 \pm 8.7
<i>GEM3D (ours)</i>	58.0 \pm 6.0	45.9 \pm 8.4	39.6 \pm 8.5

5. Conclusion

We introduce *GEM3D*, a unified representation-policy learning framework that substantially improves view-generalizable robotic manipulation. Extensive experiments demonstrate the effectiveness of our approach.

We expect this study to motivate future efforts in two directions: (i) advancing large-scale 3D pretraining with broader object collections, with the goal of learning more universal and transferable representations, and (ii) integrating distillation-based policy learning with other types of pretrained representations to learn various forms of manipulation skills.

References

[1] David Charatan, Sizhe Lester Li, Andrea Tagliasacchi, and Vincent Sitzmann. pixelsplat: 3d gaussian splats from image pairs for scalable generalizable 3d reconstruction. In *Proceedings of the IEEE/CVF conference on computer vision and pattern recognition*, pages 19457–19467, 2024. 3

[2] Shizhe Chen, Ricardo Garcia, Cordelia Schmid, and Ivan Laptev. Polarnet: 3d point clouds for language-guided robotic manipulation. *arXiv preprint arXiv:2309.15596*, 2023. 2

[3] Cheng Chi, Zhenjia Xu, Siyuan Feng, Eric Cousineau, Yilun Du, Benjamin Burchfiel, Russ Tedrake, and Shuran Song. Diffusion policy: Visuomotor policy learning via action diffusion, 2024. 2

[4] Cheng Chi, Zhenjia Xu, Chuer Pan, Eric Cousineau, Benjamin Burchfiel, Siyuan Feng, Russ Tedrake, and Shuran Song. Universal manipulation interface: In-the-wild robot teaching without in-the-wild robots, 2024. 2

[5] Özgün Çiçek, Ahmed Abdulkadir, Soeren S Lienkamp, Thomas Brox, and Olaf Ronneberger. 3d u-net: learning dense volumetric segmentation from sparse annotation. In *International conference on medical image computing and computer-assisted intervention*, pages 424–432. Springer, 2016. 4

[6] Danny Driess, Ingmar Schubert, Pete Florence, Yunzhu Li, and Marc Toussaint. Reinforcement learning with neural radiance fields. 2

[7] Ankit Goyal, Jie Xu, Yijie Guo, Valts Blukis, Yu-Wei Chao, and Dieter Fox. Rvt: Robotic view transformer for 3d object manipulation, 2023. 2

[8] Pierre-Louis Guhur, Shizhe Chen, Ricardo Garcia Pinel, Makarand Tapaswi, Ivan Laptev, and Cordelia Schmid. Instruction-driven history-aware policies for robotic manipulations. In *Conference on Robot Learning*, pages 175–187. PMLR, 2023. 2

[9] David Ha and Jürgen Schmidhuber. World models. 2018. 2

[10] Danijar Hafner, Timothy Lillicrap, and Mohammad Norouzi. Dream to control: Learning behaviors by latent imagination. 2020. 2

[11] Danijar Hafner, Timothy P. Lillicrap, Mohammad Norouzi, and Jimmy Ba. Mastering atari with discrete world models. In *International Conference on Learning Representations*, 2020. 2

[12] Nicklas Hansen, Zhecheng Yuan, Yanjie Ze, Tongzhou Mu, Aravind Rajeswaran, Hao Su, Huazhe Xu, and Xiaolong Wang. On pre-training for visuo-motor control: Revisiting a learning-from-scratch baseline. *arXiv preprint arXiv:2212.05749*, 2022. 3, 8

[13] Nicklas Hansen, Hao Su, and Xiaolong Wang. Td-mpc2: Scalable, robust world models for continuous control, 2024. 2

[14] Chengkai Hou, Yanjie Ze, Yankai Fu, Zeyu Gao, Songbo Hu, Yue Yu, Shanghang Zhang, and Huazhe Xu. 4d visual pre-training for robot learning. In *Proceedings of the IEEE/CVF International Conference on Computer Vision*, pages 8451–8461, 2025. 3

[15] Andrew Jaegle, Sebastian Borgeaud, Jean-Baptiste Alayrac, Carl Doersch, Catalin Ionescu, David Ding, Skanda Koppula, Daniel Zoran, Andrew Brock, Evan Shelhamer, et al. Perceiver io: A general architecture for structured inputs & outputs. *arXiv preprint arXiv:2107.14795*, 2021. 6

[16] Stephen James, Zicong Ma, David Rovick Arrojo, and Andrew J Davison. Rlbench: The robot learning benchmark & learning environment. *IEEE Robotics and Automation Letters*, 5(2):3019–3026, 2020. 2, 5

[17] Bernhard Kerbl, Georgios Kopanas, Thomas Leimkühler, and George Drettakis. 3d gaussian splatting for real-time radiance field rendering, 2023. 2, 3

[18] Moo Jin Kim, Karl Pertsch, Siddharth Karamcheti, Ted Xiao, Ashwin Balakrishna, Suraj Nair, Rafael Rafailov, Ethan Foster, Grace Lam, Pannag Sanketi, Quan Vuong, Thomas Kollar, Benjamin Burchfiel, Russ Tedrake, Dorsa Sadigh, Sergey Levine, Percy Liang, and Chelsea Finn. Openvla: An open-source vision-language-action model, 2024. 2

[19] Michael Laskin, Aravind Srinivas, and Pieter Abbeel. Curl: Contrastive unsupervised representations for reinforcement learning. In *Proceedings of the 37th International Conference on Machine Learning*, pages 5639–5650. PMLR, 2020. 2

[20] Yiming Li, Zhiding Yu, Christopher Choy, Chaowei Xiao, Jose M Alvarez, Sanja Fidler, Chen Feng, and Anima Anandkumar. Voxformer: Sparse voxel transformer for camera-based 3d semantic scene completion. In *Proceedings of the IEEE/CVF conference on computer vision and pattern recognition*, pages 9087–9098, 2023. 4

[21] Tsung-Yi Lin, Priya Goyal, Ross Girshick, Kaiming He, and Piotr Dollár. Focal loss for dense object detection. In *Proceedings of the IEEE international conference on computer vision*, pages 2980–2988, 2017. 5

[22] Ruoshi Liu, Rundi Wu, Basile Van Hoorick, Pavel Tokmakov, Sergey Zakharov, and Carl Vondrick. Zero-1-to-3: Zero-shot one image to 3d object. In *Proceedings of the IEEE/CVF international conference on computer vision*, pages 9298–9309, 2023. 2

[23] Guanxing Lu, Shiyi Zhang, Ziwei Wang, Changliu Liu, Jiwen Lu, and Yansong Tang. Manigaussian: Dynamic gaussian splatting for multi-task robotic manipulation, 2024. 2, 3, 6

[24] Ben Mildenhall, Pratul P. Srinivasan, Matthew Tancik, Jonathan T. Barron, Ravi Ramamoorthi, and Ren Ng. Nerf: Representing scenes as neural radiance fields for view synthesis. *Communications of the ACM*, 65(1):99–106, 2022. 2, 3

[25] Maxime Oquab, Timothée Darcet, Théo Moutakanni, Huy Vo, Marc Szafraniec, Vasil Khalidov, Pierre Fernandez, Daniel Haziza, Francisco Massa, Alaeldin El-Nouby, et al. Dinov2: Learning robust visual features without supervision. *arXiv preprint arXiv:2304.07193*, 2023. 4

[26] Yatian Pang, Eng Hock Francis Tay, Li Yuan, and Zhenghua Chen. Masked autoencoders for 3d point cloud self-supervised learning. *World Scientific Annual Review of Artificial Intelligence*, 1:2440001, 2023. 8

[27] Ben Poole, Ajay Jain, Jonathan T Barron, and Ben Mildenhall. Dreamfusion: Text-to-3d using 2d diffusion. *arXiv preprint arXiv:2209.14988*, 2022. 2

[28] Shengyi Qian, Kaichun Mo, Valts Blukis, David F. Fouhey, Dieter Fox, and Ankit Goyal. 3d-mvp: 3d multiview pre-training for robotic manipulation, 2025. 2, 3

[29] Xuanchi Ren, Yifan Lu, Hanxue Liang, Zhangjie Wu, Huan Ling, Mike Chen, Sanja Fidler, Francis Williams, and Jiahui Huang. Scube: Instant large-scale scene reconstruction using voxsplats. *Advances in Neural Information Processing Systems*, 37:97670–97698, 2024. 3

[30] Rutav Shah and Vikash Kumar. Rrl: Resnet as representation for reinforcement learning. *arXiv preprint arXiv:2107.03380*, 2021. 2

[31] Ruoxi Shi, Hansheng Chen, Zhuoyang Zhang, Minghua Liu, Chao Xu, Xinyue Wei, Linghao Chen, Chong Zeng, and Hao Su. Zero123++: a single image to consistent multi-view diffusion base model. *arXiv preprint arXiv:2310.15110*, 2023. 2

[32] Mohit Shridhar, Lucas Manuelli, and Dieter Fox. Perceiver-actor: A multi-task transformer for robotic manipulation, 2022. 2

[33] Mohit Shridhar, Lucas Manuelli, and Dieter Fox. Perceiver-actor: A multi-task transformer for robotic manipulation. In *Conference on Robot Learning*, pages 785–799. PMLR, 2023. 2, 6

[34] Stanislaw Szymanowicz, Chrisitian Rupprecht, and Andrea Vedaldi. Splatter image: Ultra-fast single-view 3d reconstruction. In *Proceedings of the IEEE/CVF conference on computer vision and pattern recognition*, pages 10208–10217, 2024. 3

[35] Jingyi Tian, Le Wang, Sanping Zhou, Sen Wang, Jiayi Li, Haowen Sun, and Wei Tang. Pdfactor: Learning tri-perspective view policy diffusion field for multi-task robotic manipulation. In *Proceedings of the Computer Vision and Pattern Recognition Conference*, pages 15757–15767, 2025. 6

[36] Che Wang, Xufang Luo, Keith Ross, and Dongsheng Li. Vrl3: A data-driven framework for visual deep reinforcement learning. *Advances in Neural Information Processing Systems*, 35:32974–32988, 2022. 3

[37] Jiaxu Wang, Qiang Zhang, Jingkai Sun, Jiahang Cao, Gang Han, Wen Zhao, Weining Zhang, Yecheng Shao, Yijie Guo, and Renjing Xu. Reinforcement learning with generalizable gaussian splatting, 2024. 2

[38] Peng Xiang, Xin Wen, Yu-Shen Liu, Yan-Pei Cao, Pengfei Wan, Wen Zheng, and Zhizhong Han. Snowflakenet: Point cloud completion by snowflake point deconvolution with skip-transformer. In *Proceedings of the IEEE/CVF international conference on computer vision*, pages 5499–5509, 2021. 2, 4

[39] Tete Xiao, Ilija Radosavovic, Trevor Darrell, and Jitendra Malik. Masked visual pre-training for motor control. *arXiv preprint arXiv:2203.06173*, 2022. 3

[40] Ge Yan, Yueh-Hua Wu, and Xiaolong Wang. Dnact: Diffusion guided multi-task 3d policy learning. *arXiv preprint arXiv:2403.04115*, 2024. 3

[41] Denis Yarats, Amy Zhang, Ilya Kostrikov, Brandon Amos, Joelle Pineau, and Rob Fergus. Improving sample efficiency in model-free reinforcement learning from images, 2020. 2

[42] Yanjie Ze, Nicklas Hansen, Yinbo Chen, Mohit Jain, and Xiaolong Wang. Visual reinforcement learning with self-supervised 3d representations. *IEEE Robotics and Automation Letters*, 8(5):2890–2897, 2023. 3

[43] Yanjie Ze, Ge Yan, Yueh-Hua Wu, Annabella Macaluso, Yuying Ge, Jianglong Ye, Nicklas Hansen, Li Erran Li, and Xiaolong Wang. Gnfactor: Multi-task real robot learning with generalizable neural feature fields. In *Proceedings of The 7th Conference on Robot Learning*, pages 284–301. PMLR, 2023. 2, 3, 6

[44] Yanjie Ze, Gu Zhang, Kangning Zhang, Chenyuan Hu, Muhan Wang, and Huazhe Xu. 3d diffusion policy: Generalizable visuomotor policy learning via simple 3d representations, 2024. 2

[45] Di Zhang, Bowen Lv, Hai Zhang, Feifan Yang, Junqiao Zhao, Hang Yu, Chang Huang, Hongtu Zhou, Chen Ye, and Changjun Jiang. Focus on what matters: Separated models for visual-based rl generalization, 2024. 2

[46] Xizhou Zhu, Weijie Su, Lewei Lu, Bin Li, Xiaogang Wang, and Jifeng Dai. Deformable detr: Deformable transformers for end-to-end object detection. *arXiv preprint arXiv:2010.04159*, 2020. 4

Learning Geometrically-Grounded 3D Visual Representations for View-Generalizable Robotic Manipulation

Supplementary Material

A. Method Details

This section provides a detailed explanation of the implementation of *GEM3D Pretraining* (see Figure 3). We also describe the training strategy and recommended hyperparameters used in the paper.

A.1. Implementation Details of 3D Feature Extractor

Given a single-view observation $o^t = \{\mathcal{I}^t, \mathcal{D}^t, \mathcal{K}^t\}$ at timestep t . The camera parameters \mathcal{K}^t consist of two parts—the extrinsic matrix: $M_{\text{extr}} = \begin{bmatrix} R & T \\ O & I \end{bmatrix}$, and the intrinsic matrix: $M_{\text{intr}} = \begin{bmatrix} f_x & 0 & c_x \\ 0 & f_y & c_y \\ 0 & 0 & 1 \end{bmatrix}$.

The depth map \mathcal{D}^t is back-projected to 3D in two steps. First, each pixel (u, v) is lifted into the camera coordinate system using the intrinsics M_{intr} :

$$\begin{bmatrix} x_c \\ y_c \\ z_c \end{bmatrix} = \begin{bmatrix} \frac{(u - c_x) \mathcal{D}^t(u, v)}{f_x} \\ \frac{(v - c_y) \mathcal{D}^t(u, v)}{f_y} \\ \mathcal{D}^t(u, v) \end{bmatrix}. \quad (1)$$

Then, the obtained 3D point is transformed into the world coordinate system using the extrinsics M_{extr} :

$$\begin{bmatrix} x \\ y \\ z \end{bmatrix} = M_{\text{extr}} \cdot \begin{bmatrix} x_c \\ y_c \\ z_c \end{bmatrix}. \quad (2)$$

Point clouds from the depth map typically contain a large amount of redundant observations (e.g., background, floor, etc.). Therefore, we first **crop** the raw point cloud and apply **farthest point sampling (FPS)** to regulate its spatial density and unify the number of points (*Note: the purpose of downsampling the point cloud to a unified number is to facilitate multi-batch parallel training*). The processed point cloud is denoted as \mathcal{P} .

However, point cloud representation is inherently unstructured, making global reconstruction and completion of occlusion part difficult to perform. To alleviate this issue, we introduce a dense volumetric intermediate representation. Specifically, each point in \mathcal{P} is assigned color information by associating it with the corresponding RGB pixel and the feature map extracted from the DinoV2. These two 3D point cloud representations are then jointly voxelized to yield volumetric observation, namely **3D Occupancy Map** and **3D Feature Map** (see Fig. 1).

Feature extraction is conducted in the voxelized space

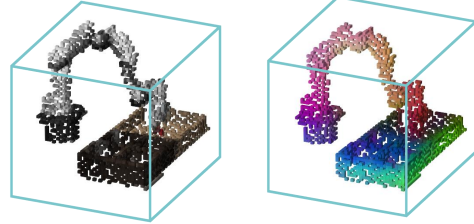


Figure 1. Volumetric observation of the Single-view input o^t . The left is the **3D Occupancy Map** of size $(d^3, 10)$, and the right is the **3D Feature Map** of size $(d^3, 384)$.

using a **fusion-style 3D U-Net**, which combines the **3D Occupancy Map** and the **3D Feature Map** to produce a spatially expanded dense volumetric feature \mathcal{F} of size $(D^3, 128)$.

The overall procedure can be summarized by the following pseudocode:

Algorithm 1: 3D Feature Extractor

Input: $\mathcal{I}^t, \mathcal{D}^t, \mathcal{K}^t = \{M_{\text{extr}}, M_{\text{intr}}\}$
Output: Dense volumetric feature \mathcal{F}
 $\mathcal{F}_{2D} \leftarrow \text{DinoV2}(\mathcal{I}^t) \quad // (H \times W, 384)$
 $P_{\text{raw}} \leftarrow \text{PIXEL2POINT}(\mathcal{D}^t, \mathcal{K}^t) \quad // \text{Eq. 1, Eq. 2}$
 $P_{\text{crop}} \leftarrow \text{CROP}(P_{\text{raw}})$
 $P \leftarrow \text{FPS}(P_{\text{crop}}, N)$
 $(V_{\text{occ}}, V_{\text{feat}}) \leftarrow \text{VOXELIZE}(P, \mathcal{I}^t, \mathcal{F}_{2D}) \quad // (D^3, 10),$
 $(D^3, 384)$
 $\mathcal{F} \leftarrow \text{3D UNet}(V_{\text{occ}}, V_{\text{feat}}) \quad // (D^3, 128)$
return \mathcal{F}

A.2. Implementation Details of 3D Deformable Attention

In our **coarse-to-fine point cloud reconstruction** module, we adopt a **3D Deformable Cross-Attention (DCA)** mechanism operating over voxel proposal queries. Specifically, the input x corresponds to the *proposal voxel queries* $\mathcal{Q}_p \in \mathbb{R}^{d^3 \times C}$ from the preceding stage, where d^3 is the number of voxel tokens and C is the channel dimension (here $C = 128$). The optional context features are provided by the dense volumetric feature \mathcal{F} extracted from the fusion-style 3D U-Net.

For each voxel query token $\mathbf{q}_p \in \mathcal{Q}_p$, the module predicts a set of learnable offsets $\{\Delta \mathbf{p}_k(\mathbf{q}_p)\}_{k=1}^{N_p}$ around a reference voxel position \mathbf{p}_0 , forming a *voxel-wise sampling grid* v_{grid} . Keys and values are then sampled from \mathcal{F} at these locations using $\mathcal{F}.\text{grid_sample}$, and attention weights

$A_k(\mathbf{q}_p)$ are computed to aggregate local geometric information. The refined token feature, referred to as the *seed token*, is obtained as:

$$\text{DCA}(\mathbf{q}_p, \mathcal{F}) = \frac{1}{N_p} \sum_{k=1}^{N_p} A_k(\mathbf{q}_p) \mathcal{F}(\mathbf{p}_0 + \Delta \mathbf{p}_k(\mathbf{q}_p)). \quad (3)$$

To enhance 3D geometric awareness, a **continuous positional bias (CPB)** is integrated. For each query voxel token \mathbf{q}_p and its sampled locations $\mathbf{p}_0 + \Delta \mathbf{p}_k(\mathbf{q}_p)$, CPB produces a learnable bias

$$b_{p,k} = \text{CPB}(\mathbf{q}_p, \mathbf{p}_0 + \Delta \mathbf{p}_k(\mathbf{q}_p)), \quad (4)$$

which is directly added to the raw attention logits before normalization:

$$\tilde{A}_k(\mathbf{q}_p) = \text{softmax}(A_k(\mathbf{q}_p) + b_{p,k}). \quad (5)$$

Together with the learned offsets, this allows DCA to selectively aggregate features from spatially relevant voxels, efficiently refining each voxel token with precise local geometric context. In essence, CPB provides a learnable bias that modulates attention weights based on relative 3D positions.

Compared to standard full-grid 3D cross-attention, which has complexity $O(N_p \cdot D^3 \cdot C)$ for N_p queries and D^3 voxels, DCA reduces both memory and computation to $O(N_p^2 \cdot C)$ by attending only to $N_p \ll D^3$ sampled locations per token while preserving fine-grained local details.

Below is the implementation procedure of 3D DCA.

Algorithm 2: 3D Deformable Cross-Attention

Input: Voxel proposal queries $\mathcal{Q}_p \in \mathbb{R}^{d^3 \times C}$, dense volumetric feature \mathcal{F} , number of offsets N_p
Output: Refined voxel tokens $\mathcal{Q}_p^{\text{refined}}$

$$\{\Delta \mathbf{p}_k(\mathbf{q}_p)\}_{k=1}^{N_p} \leftarrow \text{OFFSETPREDICTOR}(\mathcal{Q}_p) //$$

Learnable offsets per voxel token

$$\mathbf{p}_k \leftarrow \mathbf{p}_0 + \Delta \mathbf{p}_k(\mathbf{q}_p) //$$

Sampling locations in 3D voxel space

$$K, V \leftarrow \mathcal{F}.\text{grid_sample}(\mathcal{F}, \mathbf{p}_k) //$$

Extract voxel features at sampled offsets

$$A_k(\mathbf{q}_p) \leftarrow \text{SOFTMAX}(\langle \mathbf{q}_p, K \rangle + \text{CPB}(\mathbf{q}_p, \mathbf{p}_k)) //$$

Continuous positional bias modulates attention

$$\mathcal{Q}_p^{\text{refined}} \leftarrow \frac{1}{N_p} \sum_{k=1}^{N_p} A_k(\mathbf{q}_p) V_k //$$

Seed tokens capturing local geometry

return $\mathcal{Q}_p^{\text{refined}}$

Design Highlights of 3D DCA:

- Adaptive offsets enable attention to focus on locally informative voxels rather than uniform grids.
- Dense voxel features are queried via the voxel-wise sampling grid using $\mathcal{F}.\text{grid_sample}$, enabling efficient aggregation of local geometric information from the volumetric feature field to each proposal voxel query.
- Continuous positional bias (CPB) encodes relative 3D po-

sitions, improving spatial reasoning and guiding attention toward geometrically relevant locations.

A.3. Training Details

A.3.1. Training Details for *GEM3D Pretraining*

Training on robotic scenes with extremely large variance is inherently challenging. In the ablation study (Fig. 6 in the main paper), we have visually demonstrated the *GEM3D Pretraining* module that influence reconstruction and rendering quality.

But in practice, we additionally adopt several training techniques that are admittedly heuristic but not novel enough to be presented as core contributions in the main paper. However, these strategies are essential for stable reconstruction. In particular, in order to enable *GEM3D Pretraining* to perform feed-forward Gaussian splatting, we employ a series of optimization strategies that are substantially different from traditional 3D Gaussian Splatting. We summarize our key practical insights as follows:

- *Stage-wise decoupled reconstruction and rendering.* Previous works have pointed out that the quality of Gaussian splatting reconstruction heavily depends on the initialization of point positions. Conventional 3D Gaussian Splatting often relies on Gaussian point cloud initialized from COLMAP. Similarly, during training, the rendering stage (c) strongly depends on the reconstruction quality of stage (b), especially when both modules share the same feature representation \mathcal{F} to simultaneously solve two related but distinct tasks: geometry reconstruction and novel view synthesis.

If novel view rendering is enforced too early while the reconstruction quality is still poor, the gradients from stage (c) may negatively interfere with the learning of \mathcal{F} , leading to unstable convergence and even complete collapse of the reconstructed scene. Therefore, during the first δ **training iterations**, we exclusively optimize the reconstruction objective of stage (b) and completely disable the rendering module (c). Only after reliable geometric and appearance-consistent point clouds can be recovered from \mathcal{F} do we enable stage (c) and allow gradients from novel-view rendering to be back-propagated. This strategy provides a stable geometric prior for subsequent Gaussian splatting.

- *Multi-step iterative reconstruction per scene.* A fundamental difference between feed-forward Gaussian splatting and traditional optimization-based splatting lies in the need for strong cross-scene generalization. In the early training phase, directly switching to a new scene after a single gradient update often leads to reconstruction failure due to large scene variance.

To mitigate this issue, we perform **k consecutive optimization steps** on the same scene before switching to the next one. As training progresses and the model becomes

more stable, we gradually decrease k until it eventually becomes 1, corresponding to standard single-step updates per scene.

A.3.2. Training Strategy for *GEM3D Policy*

During policy learning, imitation is performed from human demonstrations. However, raw trajectories often contain redundant intermediate states (e.g., gripper approaching motions). We therefore select a sparse set of keyframes that correspond to interaction-critical states.

Given a demonstration trajectory

$$\mathcal{D} = \{o_t\}_{t=1}^T,$$

where $g_t \in \{0, 1\}$ denotes the gripper open/close state, a timestep t is selected as a keyframe if

$$t \in \mathcal{K} \iff (g_t \neq g_{t-1}) \vee (t = T) \vee \text{STOPPED}(o_t), \quad (6)$$

where $\text{STOPPED}(\cdot)$ indicates near-static motion under a small velocity threshold. Redundant adjacent keyframes are further removed.

This strategy significantly shortens the demonstration sequence while preserving states that are critical for object interaction.

A.4. Parameters Details

Table 1. Key Hyperparameters of *GEM3D Pretraining*

Parameters	Value
train.batch_size	1
train.learning_rate	1.0×10^{-4}
train.optimizer	torch.optim.AdamW
train.steps	100K
train.num_views	8
train. δ	40K
train.k	[4, 3, 2, 1]
train.demos	50
network.D	100
network.d	[7, 7, 7]
network.fps_sample_num	512
network.scene_bounds	[-0.375, -0.5, 0.6, 1.0, 0.5, 1.6]

Table 2. Key Hyperparameters of *GEM3D Policy*

Parameters	Value
train.batch_size	1
train.learning_rate	1.0×10^{-4}
train.optimizer	torch.optim.AdamW
train.single_task_steps	12K
train.camera	[front]
train.demos	20
network.scene_bounds	[-0.375, -0.5, 0.6, 1.0, 0.5, 1.6]
network.num_tokens	8000
network.num_latents	2048
network. $\lambda_{distill}$	[1, 0.5, 0.3, 0.2, 0.1, 0.05]

B. Tasks Description

We selected 12 tasks from RLBench, which together contain 178 variations. See Fig. 2 and Table 3 for detail description.

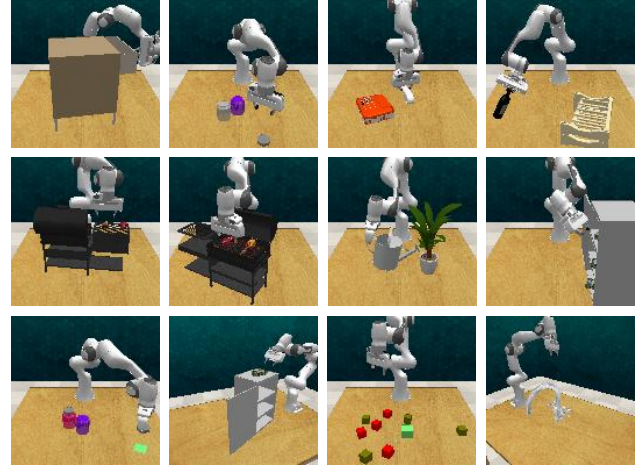


Figure 2. RLBench tasks. 12 tasks of 9 scenes are selected.

Notably, among these 12 tasks, close jar and open jar, meat off grill and meat on grill, put money in safe and take money out safe belong to the same scene but involve different action trajectories. Thus, these 12 tasks only cover 9 distinct scenes, and during pretraining, we only collected tasks from just 9 tasks to cover all of the scenes. This task design aims to evaluate the generalization capability of *GEM3D*.

Specifically, the trajectories for open jar, meat on grill, and take money out safe were not seen during pretraining. Nevertheless, Table 1 in the main paper demonstrates that *GEM3D* still improves performance on these extrapolated tasks. Table 2 in main paper further shows that even for tasks with different trajectories within the same scene, our method enhances viewpoint generalization on extrapolated tasks. This indicates that although the pretrained model has not encountered new viewpoints in these tasks, single-view expert demonstrations during policy learning are sufficient to achieve significant improvements in novel viewpoints —it highlights that the pretrained representation effectively captures scene-level geometric features, enabling new skill adaptation and continual learning in real-world monocular system deployments.

C. Supplementary of Experiments

C.1. Additional Details of Manipulation Tasks

Table 2 in the main paper reports results on six representative tasks. We further evaluate two additional heavily occluded tasks, open drawer and take money out safe, in Table 4. We observe that performance drops more noticeably under viewpoint changes for these tasks, especially under the large-shift setting, where execution almost

Table 3. Task Descriptions. The 12 highly challenging tasks include a variety of random variations in color and layout, as well as multiple language instruction variations.

Task	Type	Variations	Instruction Template
Close Jar	color	20	“close the _jar”
Open Drawer	placement	3	“open the _drawer”
Meat off Grill	size	2	“take the _off the grill”
Turn Tap	category	2	“turn _tap”
Water Plants	placement	1	“water plant”
Phone on Base	placement	1	“put the phone on the base”
Put Money in Safe	placement	3	“put the money away in the safe on the _shelf”
Place Wine	placement	1	“stack wine bottle”
Stack Blocks	color, count	60	“stack _ _ blocks”
Open Jar	color	80	“open the _jar”
Meat on Grill	category	2	“put the _on the grill”
Take Money out Safe	placement	3	“take the money out of the _shelf and place it on the table.”

completely fails. This is because, under large shifts, one side of the scene is nearly entirely occluded (as shown in Fig. 3), leading to severe inconsistencies in visual representations across viewpoints, which the model cannot effectively resolve, ultimately causing execution collapse. It shows that *GEM3D* still relies on the visibility of essential contact details during manipulation.

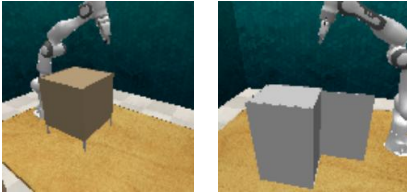


Figure 3. open drawer and take money out safe tasks in large view shift. Both of the tasks suffer the severe occlusion, resulting drastic success rate drop.

Additionally, we provide a more detailed analysis of the multi-task setting reported in Table 3 of the main paper. Table 5 reports the per-task success rates under multi-task training, together with the relative performance changes compared to the single-task setting.

C.2. More Rendering Results

In the main paper, we present qualitative visualizations on the tasks of open drawer, turn tap, and water plants, and quantitatively evaluate the PSNR and SSIM metrics for novel view synthesis. Specifically, for all keyframe sequences, we synthesize novel views from 18 uniformly distributed virtual cameras under 8 supervised viewpoints. In this section, we provide more demonstrations of novel view synthesis results. (See Fig. 4, Fig. 5)

Table 4. Result of zero-shot view generalization on eight RLBench tasks under two view-shift settings (SR%). **Bold** numbers denote the best performance, and \downarrow indicates the relative performance drop compared to the training view.

	Methods	Close Jar	Meat off Grill	Turn Tap	Phone on Base	Open Jar	Meat on Grill	Open Drawer	Take Money out Safe	Avg.
Train View	<i>PerAct</i>	19.0 \pm 4.6	28.3 \pm 4.7	43.7 \pm 4.7	51.3 \pm 11.9	26.7 \pm 9.1	16.0 \pm 7.9	38.7 \pm 13.7	13.7 \pm 2.9	29.7 \pm 13.7
	<i>ManiGaussian</i>	27.3 \pm 16.4	30.0 \pm 11.3	44.0 \pm 10.5	66.3 \pm 12.5	38.3 \pm 9.0	50.7 \pm 12.9	57.3 \pm 1.5	49.3 \pm 10.5	42.9 \pm 14.0
	<i>ManiGaussian</i> (<i>w Distill</i>)	31.0 \pm 12.1	35.3 \pm 9.8	42.7 \pm 14.6	64.3 \pm 16.2	33.7 \pm 9.5	48.7 \pm 2.9	54.3 \pm 12.5	43.0 \pm 23.4	44.1 \pm 11.3
	GEM3D (<i>ours</i>)	44.7 \pm 3.2	44.3 \pm 3.1	56.0 \pm 7.2	67.3 \pm 1.5	40.0 \pm 5.6	61.0 \pm 22.1	65.7 \pm 4.5	72.0 \pm 13.7	56.4 \pm 12.1
Moderate Shift	<i>PerAct</i>	7.7 \pm 9.9 (59.65% \downarrow)	19.7 \pm 7.2 (30.56% \downarrow)	14.0 \pm 7.2 (67.94% \downarrow)	0.3 \pm 0.6 (99.35% \downarrow)	2.0 \pm 1.7 (92.50% \downarrow)	12.3 \pm 9.6 (22.92% \downarrow)	19.7 \pm 7.2 (49.14% \downarrow)	3.3 \pm 3.2 (75.61% \downarrow)	9.9 \pm 7.7 (62.21% \downarrow)
	<i>ManiGaussian</i>	15.3 \pm 15.9 (43.91% \downarrow)	17.0 \pm 12.1 (43.33% \downarrow)	32.3 \pm 2.3 (26.52% \downarrow)	30.7 \pm 18.6 (53.76% \downarrow)	18.3 \pm 2.5 (52.18% \downarrow)	24.3 \pm 10.1 (20.67% \downarrow)	30.3 \pm 18.0 (47.09% \downarrow)	12.0 \pm 4.4 (75.67% \downarrow)	22.5 \pm 7.9 (45.39% \downarrow)
	<i>ManiGaussian</i> (<i>w Distill</i>)	20.3 \pm 10.3 (34.41% \downarrow)	23.7 \pm 2.3 (33.01% \downarrow)	34.0 \pm 9.8 (20.32% \downarrow)	40.0 \pm 22.6 (37.82% \downarrow)	21.7 \pm 3.2 (35.64% \downarrow)	42.3 \pm 7.0 (13.02% \downarrow)	31.7 \pm 4.5 (41.71% \downarrow)	21.0 \pm 14.8 (51.16% \downarrow)	29.3 \pm 8.9 (33.39% \downarrow)
	GEM3D (<i>ours</i>)	33.7 \pm 8.5 (24.62% \downarrow)	33.0 \pm 5.0 (25.56% \downarrow)	47.7 \pm 8.4 (14.88% \downarrow)	48.3 \pm 13.6 (28.22% \downarrow)	34.3 \pm 4.0 (14.18% \downarrow)	47.0 \pm 14.8 (22.95% \downarrow)	42.7 \pm 9.5 (35.02% \downarrow)	41.7 \pm 13.6 (42.13% \downarrow)	41.0 \pm 6.5 (25.95% \downarrow)
Large Shift	<i>PerAct</i>	2.8 \pm 3.4 (85.11% \downarrow)	15.7 \pm 3.1 (44.69% \downarrow)	9.7 \pm 4.3 (77.86% \downarrow)	1.0 \pm 2.0 (98.05% \downarrow)	3.3 \pm 4.1 (87.51% \downarrow)	4.8 \pm 3.8 (69.81% \downarrow)	1.5 \pm 1.9 (96.12% \downarrow)	1.2 \pm 2.4 (91.44% \downarrow)	5.0 \pm 5.2 (81.32% \downarrow)
	<i>ManiGaussian</i>	10.3 \pm 14.2 (62.20% \downarrow)	16.3 \pm 8.4 (45.57% \downarrow)	27.0 \pm 7.0 (38.64% \downarrow)	23.7 \pm 16.0 (64.32% \downarrow)	21.5 \pm 6.9 (43.91% \downarrow)	16.0 \pm 6.2 (47.83% \downarrow)	0.0 \pm 0.0 (100.00% \downarrow)	1.3 \pm 1.8 (97.30% \downarrow)	14.5 \pm 10.0 (62.47% \downarrow)
	<i>ManiGaussian</i> (<i>w Distill</i>)	21.5 \pm 9.2 (45.16% \downarrow)	16.3 \pm 6.9 (67.92% \downarrow)	32.0 \pm 8.6 (29.69% \downarrow)	33.7 \pm 13.1 (41.97% \downarrow)	23.2 \pm 12.0 (62.38% \downarrow)	28.2 \pm 8.0 (53.42% \downarrow)	0.7 \pm 1.2 (98.77% \downarrow)	5.3 \pm 7.4 (87.60% \downarrow)	20.1 \pm 12.0 (60.86% \downarrow)
	GEM3D (<i>ours</i>)	30.2 \pm 7.1 (32.46% \downarrow)	26.0 \pm 5.8 (41.35% \downarrow)	45.3 \pm 6.3 (19.05% \downarrow)	39.0 \pm 13.2 (42.08% \downarrow)	35.8 \pm 7.7 (10.42% \downarrow)	40.3 \pm 6.8 (33.88% \downarrow)	11.0 \pm 15.0 (83.25% \downarrow)	8.2 \pm 10.0 (88.56% \downarrow)	29.5 \pm 13.7 (43.88% \downarrow)

Table 5. Result of Multi-task view generalization on RLBench tasks. We report the success rate (mean \pm std %) in the Multi-task setting. **Bold** numbers denote the best performance. The percentage in parentheses indicates the relative performance change compared to the Single-task baseline ($\frac{\text{Multi-Single}}{\text{Single}}$).

	Methods	Open Jar	Meat on Grill	Turn Tap	Phone on Base	Avg.
Moderate Shift	<i>PerAct</i>	4.3 \pm 4.0 (115.00% \uparrow)	2.0 \pm 2.6 (83.74% \downarrow)	15.7 \pm 5.0 (12.14% \uparrow)	3.7 \pm 6.4 (1133.33% \uparrow)	6.4 \pm 4.5 (11.11% \downarrow)
	<i>ManiGaussian</i> (<i>w Distill</i>)	21.0 \pm 7.9 (3.23% \downarrow)	28.7 \pm 10.1 (32.15% \downarrow)	44.3 \pm 9.1 (30.29% \uparrow)	28.7 \pm 5.1 (28.25% \downarrow)	30.7 \pm 8.1 (11.01% \downarrow)
	GEM3D (<i>ours</i>)	27.0 \pm 13.0 (21.28% \downarrow)	38.7 \pm 14.5 (17.66% \downarrow)	59.0 \pm 4.6 (23.69% \uparrow)	40.0 \pm 6.2 (17.18% \downarrow)	41.2 \pm 9.6 (7.00% \downarrow)
	<i>PerAct</i>	5.3 \pm 5.2 (60.61% \uparrow)	1.2 \pm 1.9 (75.00% \downarrow)	14.5 \pm 5.4 (49.48% \uparrow)	1.5 \pm 1.8 (50.00% \uparrow)	5.6 \pm 3.6 (19.15% \uparrow)
Large Shift	<i>ManiGaussian</i> (<i>w Distill</i>)	22.2 \pm 7.2 (16.23% \downarrow)	26.3 \pm 9.3 (6.05% \uparrow)	36.0 \pm 10.2 (20.00% \uparrow)	21.3 \pm 5.7 (42.90% \downarrow)	26.5 \pm 8.1 (10.77% \downarrow)
	GEM3D (<i>ours</i>)	27.0 \pm 10.7 (9.40% \downarrow)	31.3 \pm 7.4 (15.86% \downarrow)	47.0 \pm 12.6 (3.75% \uparrow)	40.3 \pm 5.4 (3.33% \uparrow)	36.4 \pm 9.0 (3.70% \downarrow)

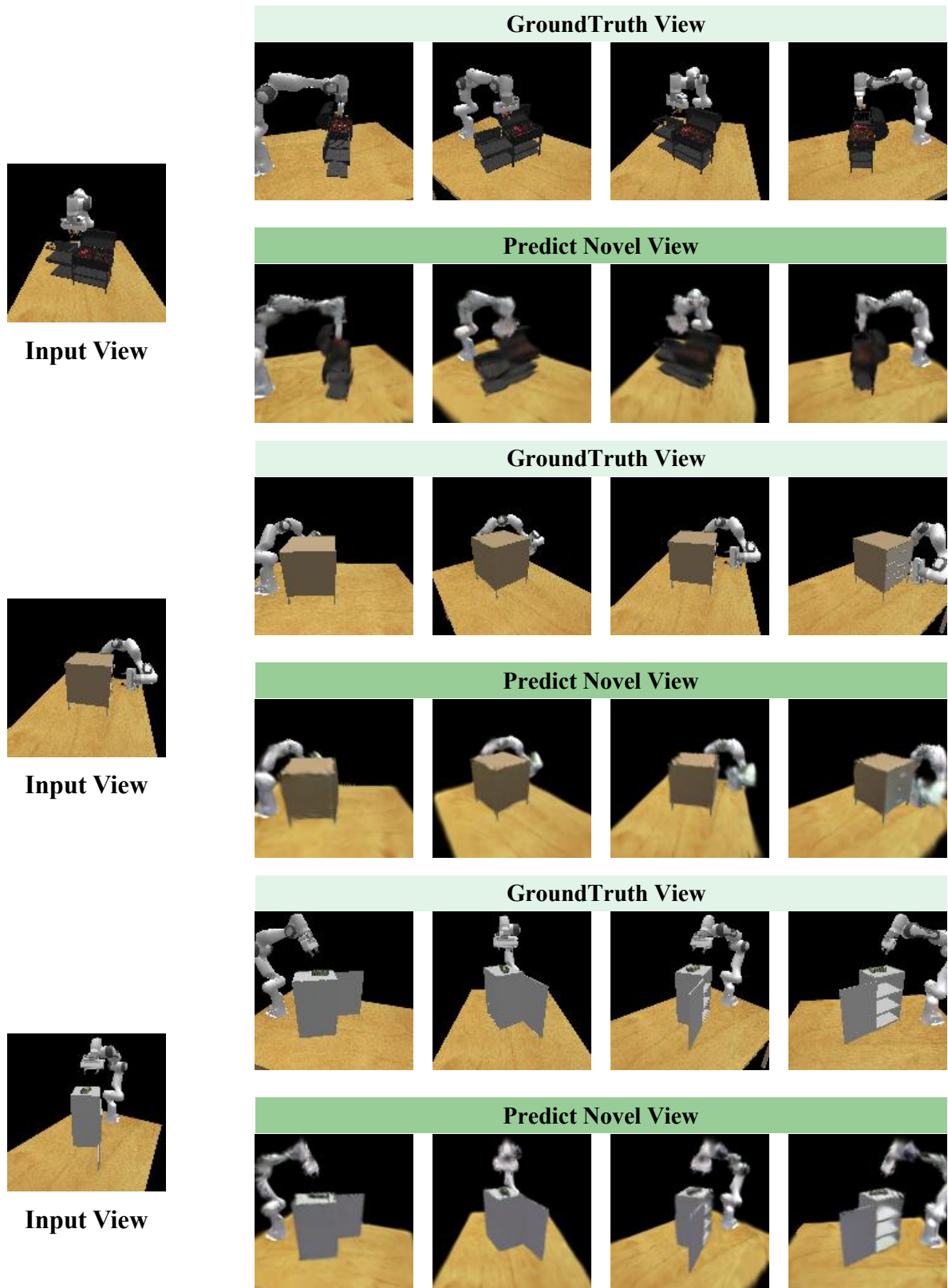


Figure 4. Rendering Results (Part 1/2).

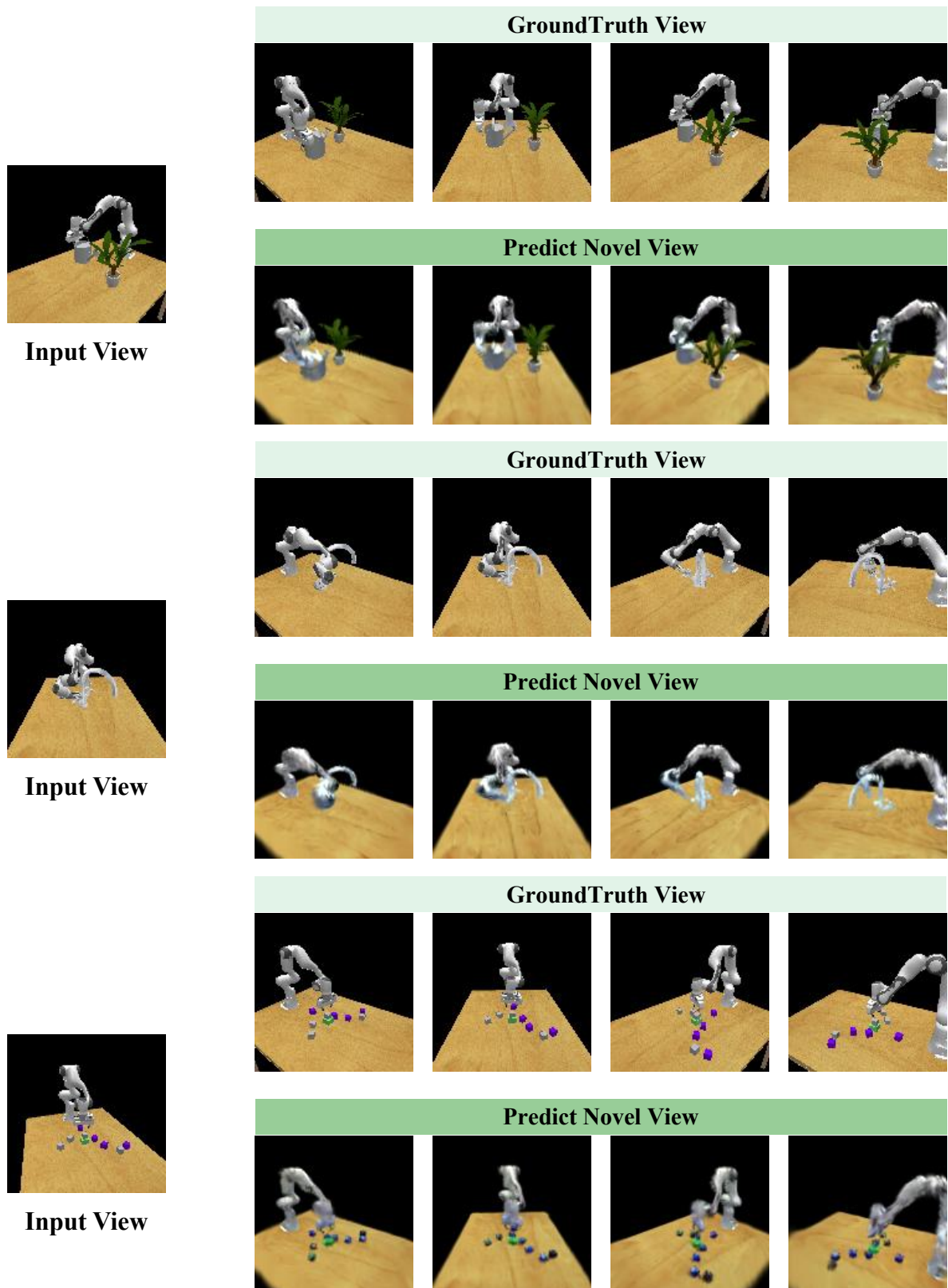


Figure 5. Rendering Results (Part 2/2).